Observation of orbital angular momentum in the chiral magnet CrNb_{3}S_{6} by soft x-ray magnetic circular dichroism

M. Mito, H. Ohsumi, T. Shishidou, F. Kuroda, M. Weinert, K. Tsuruta, Y. Kotani, T. Nakamura, Y. Togawa, J. Kishine, Y. Kousaka, J. Akimitsu, and K. Inoue

Phys. Rev. B **99**, 174439 — Published 29 May 2019

DOI: 10.1103/PhysRevB.99.174439

Observation of orbital angular momentum in the chiral magnet $CrNb_3S_6$ by soft x-ray magnetic circular dichroism

M. Mito[1,2],* H. Ohsumi[3], T. Shishidou[4],† F. Kuroda[5], M. Weinert[4], K. Tsuruta[6], Y. Kotani[6], T. Nakamura[6], Y. Togawa[2,7], J. Kishine[2,8], Y. Kousaka[2,9], J. Akimitsu[9], and K. Inoue[2,10,11]

[1] *Graduate School of Engineering, Kyushu Institute of Technology, Kitakyushu 804-8550, Japan*
[2] *Center for Chiral Science, Hiroshima University, Higashihiroshima 739-8526, Japan*
[3] *RIKEN SPring-8 Center, Hyogo 679-5148, Japan*
[4] *Department of Physics, University of Wisconsin-Milwaukee, Milwaukee, Wisconsin 53201, USA*
[5] *Institute of Scientific and Industrial Research, Osaka University, Osaka 567-0047, Japan*
[6] *Japan Synchrotron Radiation Research Institute (JASRI), Hyogo 679-5198, Japan*
[7] *Graduate School of Engineering, Osaka Prefecture University, Sakai 599-8570, Japan*
[8] *Graduate School of Arts and Sciences, The Open University of Japan, Chiba 261-8586, Japan*
[9] *Research Institute for Interdisciplinary Science, Okayama University, Okayama 700-8530, Japan*
[10] *Graduate School of Science, Hiroshima University, Higashihiroshima 739-8526, Japan and*
[11] *Institute for Advanced Materials Research, Hiroshima University, Higashihiroshima 739-8526, Japan*

(Dated: May 14, 2019)

The chiral magnet $CrNb_3S_6$ with its solitonic objects has novel magnetic and transport properties, in which the spin-orbit coupling (SOC) plays a central role. Aiming to address the possible existence of orbital moments driven by SOC, we perform soft x-ray magnetic circular dichroism spectroscopy at the Cr $L_{2,3}$ edges with in-plane magnetization. The dichroic signals provide direct experimental evidence that the Cr orbital magnetic moment is not quenched and is coupled antiparallel to the spin counterpart. Application of the orbital sum rule reveals that the magnitude of the Cr orbital moment is about 1 % of the total magnetization. These findings are consistent with the first-principles electronic structure calculations that utilize the Cr $2p$ core radial function to define the Cr local $3d$ quantities. The distinct roles of the atomic SOC among the Cr $3d$ and Nb $4d$ states are discussed.

PACS numbers:

I. INTRODUCTION

The monoaxial chiral helimagnet $CrNb_3S_6$ has attracted intensive interest with regard to its solitonic spin texture. The Dzyaloshinskii-Moriya (DM) interaction[1,2], driven by the spin-orbit coupling (SOC) and crystalline chirality, leads to intriguing phenomena. The magnetic ground state is a long-wavelength spiral order of Cr spins: magnetic moments, aligned ferromagnetically in the hexagonal ab plane, form a magnetic helix along the c axis with the handedness imprinted by the crystal chirality. Applying a relatively small magnetic field H perpendicular to the c axis drastically changes the magnetic configuration from a homogeneous spiral to the soliton kink structure – termed the chiral soliton lattice (CSL)[3–5] – and eventually to the forced ferromagnetic (FM) state at a critical magnetic field H_c of a few kOe[6]. Negative magnetoresistance has been observed in the CSL phase[7,8].

In $CrNb_3S_6$, Cr atoms intercalate in the layered parent $2H_a$-NbS_2 compound forming a planar $\sqrt{3}\times\sqrt{3}$ super structure (see Fig. 1(a)). The stacking sequence along the c axis – whether the Cr atoms occupy $2d$ or $2c$ Wyckoff sites in the Sohncke[9,10] space group $P6_322$ – determines the crystalline chirality. Nb atoms split into two groups, those preserving their ideal positions ($2a$ site) and those with their z coordinates slightly deviating from 0 or 1/2 ($4f$ site), as shown in Table I. Each Cr has six nearest-neighbor sulfurs and two Nb ($4f$) atoms at distances of 2.35 and 3.06 Å, respectively (see Figs. 1(a,b))[11]. In this cluster unit CrS_6-Nb_2 the local symmetry around Cr is approximately D_{3d} and the Cr $3d$ orbitals show an energy splitting $t_{2g}\rightarrow e'_g+a_{1g}$ as in Fig. 1(c). (Although the actual site symmetry is D_3, we will use this notation to be consistent with previous work.) Here a_{1g} is a $3z^2-r^2$ orbital aligned along the c axis toward Nb ($4f$) atoms. A localized picture with electron configuration $(t_{2g})^3$ [or $(e'_g)^2(a_{1g})^1$] with a nominal valency Cr^{3+} is often considered since it provides a local moment S=3/2 consistent with the observed magnetic moment ∼3 μ_B [2.9 μ_B[6], 3.2 μ_B[12]].

Provided that the SOC is weak compared to other interactions (e.g., crystalline field, orbital hybridization, and exchange interaction), the DM interaction arises from a combined second-order perturbation of the SOC and (twisted) exchange interaction, and thus the DM is linear in SOC. On the other hand, magnetocrystalline anisotropy (MCA) and unquenched orbital magnetic moments arise from SOC alone. In $CrNb_3S_6$, although the MCA has been known to be easy-plane type[6], the orbital magnetic moment has never been measured experimentally. Indeed, the magnetic ordering temperature T_c of $CrNb_3S_6$ was evaluated to be approximately 130 K[6,11,13]. Recently, the interplane exchange interaction along the chiral c axis ($J_\parallel/k_B = 16.2$ K), the DM interaction (D/k_B = 1.29 K), and the easy-plane anisotropy (K_{perp}/k_B = 1.02 K) have been evaluated from the ESR experiment[14], showing fair agreement with the estimated values from the magnetization curve[15]. It is expected that analyzing

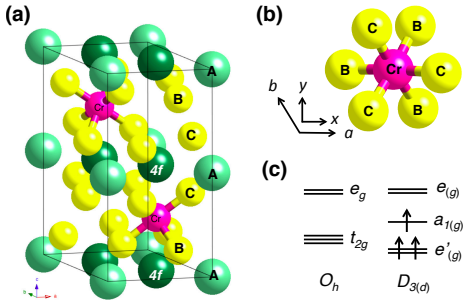

FIG. 1: (a) Crystal structure of $CrNb_3S_6$. The host NbS_2 forms a two-dimensional triangular layer with S-Nb-S stacking sequence of (B-A-B) (C-A-C) (B-A-B) $\cdots$. There are two Cr atoms per unit cell (shown by red spheres), which occupy the $2d$ site. Nb atoms at a $4f$ site are drawn by dark green. (b) Top view of CrS_6 cluster with definition of planar axes. (c) Crystalline field splitting of Cr $3d$ level.

these quantities will reveal how the SOC manifests itself in $CrNb_3S_6$ and further would provide a clue to understand the microscopic origin of the DM interaction.

Here we report x-ray magnetic circular dichroism (XMCD) measurements at the Cr $L_{2,3}$ edges ($2p \rightarrow 3d$ photoabsorption) in the forced FM state with the external field perpendicular to the c axis. Utilizing the Cr $2p$ core state, which is highly localized around the nucleus, as a local probe, the XMCD measurement provides direct information about the Cr local spin and orbital magnetic moments induced in the Cr $3d$ shell. It is found that the $3d$ orbital moment is small but finite and is coupled antiparallel to the spin counterpart, consistent with the density functional theory (DFT) calculations that we report here.

Both in the experimental and theoretical studies we carry out, quantitative determination of the Cr $3d$ spin and orbital moments is, however, not straightforward. The so-called XMCD spin sum rule[16] is not directly applicable to the present case: Cr is a light transition-metal atom and its $2p$ core spin-orbit splitting (~ 8 eV) is not large enough to prevent quantum mechanical mixing between the $2p_{3/2}$ and $2p_{1/2}$ excitations (j-j mixing) caused by the $2p$-$3d$ Coulomb interaction in the photoabsorption final states[17]. Thus the fundamental assumption behind the spin sum rule – that the L_3 and L_2 edges are well separated in energy and identified as pure $2p_{3/2}$ and $2p_{1/2}$ excitations respectively – is violated to a considerable extent. We examine a correction method[18] proposed by Goering for the spin sum rule that uses the branching ratio of the L_2 to L_3 edges in the x-ray absorption spectrum (XAS) for unpolarized light (i.e., 2/4 in the no mixing case), but find it is unsuccessful in the present case. Furthermore, the effective magnetic moment per mole of Cr atoms calculated from the Curie constant is approximately 4 μ_B [3.92 μ_B[6], 4.4 μ_B[12], 4.1-4.3 μ_B[19]]. As for the number of holes in the $3d$ shell (n_h), the nominal value of $n_h = 7$ is unreasonable, and we therefore use DFT calculations to derive optimal n_h values.

TABLE I: Structural parameters of $CrNb_3S_6$ taken from Ref. 11.

Space group #182, $P6_322$,	a=5.7134 Å,	c=12.0563 Å
Element	Wyckoff	Internal position
Cr	$2d$	(2/3, 1/3, 1/4)
Nb	$2a$	(0,0,1/2)
Nb	$4f$	(1/3, 2/3, 0.4962)
S	$12i$	(0.31836, -0.01252, 0.63263)

On the other hand, the orbital sum rule[20], which does not rely on a distinction between the L_3 and L_2 edges, should be applicable to the present case. Our main focus in the XMCD measurement is, therefore, the evaluation of the Cr $3d$ orbital moment. Nevertheless, care is needed in applying either of these sum rules since both are vulnerable to errors in the normalization and background correction to the absorption intensity.

In the DFT calculations, the information regarding the spin and orbital moments is provided as a density distribution calculated from a corresponding operator $\mathbf{A}$ and band spinors $\psi_i(\mathbf{r})$, $\mathbf{A}(\mathbf{r}) = \sum_i \psi_i^\dagger \mathbf{A} \psi_i$ which is a continuous function of $\mathbf{r}$. The idea of atomic-like Cr local moments is ill-defined since their values depend on the region used to integrate $\mathbf{A}(\mathbf{r})$. Furthermore, there is strong hybridization of Cr $3d$ states with S $3p$ and Nb $4d$ states that makes the separation of a Cr $3d$ shell ill-defined. To cope with these difficulties, we resort to the fact that the Cr $L_{2,3}$ XAS/XMCD measurements employ the Cr $2p$ core state as a local probe to detect the Cr $3d$ states, and develop a method to define and calculate the Cr $3d$ components in the DFT orbitals $\psi_i(\mathbf{r})$ through a projection on to the Cr $2p$ core wave functions, mimicking the experimental situation.

The rest of this paper is organized as follows. In Section II, the XAS/XMCD sum rules are reviewed, and from there, the definition of Cr local $3d$ quantities used in the DFT calculations is provided. Section III is devoted to describe experimental procedures. In Section IV, XMCD results at the Cr $L_{2,3}$ edges are provided, and in Section V, the DFT results are shown. Section VI provides concluding remarks.

II. $3d$ MOMENTS PROBED BY $2p$ CORE STATES

Consider the electric-dipole (E1) transition from the Cr $2p$ core to the Cr $3d$ valence shell. Assume that these states are expressed by *single* normalized radial functions, R_i (i=$2p$, $3d$), $\langle R_i | R_i \rangle$=1, ignoring their energy dependency. Starting from the Fermi golden rule for the E1 transition and applying the Wigner-Eckart theorem,

it can be shown[16,20] that the integrated photo-excitation spectra are related to the orbital and spin magnetic moments of the Cr $3d$ shell ($m_{\rm orb}$ and $m_{\rm spin}$ in unit of $\mu_{\rm B}$):

$$\int(\mu_+ - \mu_-)d\omega = \frac{1}{2}\,\kappa\; m_{\rm orb}, \tag{1}$$

$$\int_{j_+}(\mu_+ - \mu_-)d\omega - 2\int_{j_-}(\mu_+ - \mu_-)d\omega = \frac{1}{3}\,\kappa\; m_{\rm spin}, \tag{2}$$

$$\int(\mu_+ + \mu_- + \mu_0)d\omega = \kappa\; n_{\rm h} \tag{3}$$

where μ_+ and μ_- denote absorption coefficients of circularly polarized x-rays that propagate along the magnetization direction with positive and negative helicities (σ_+ and σ_-), respectively, μ_0 for x-rays linearly polarized along the magnetization direction, and κ is a normalization constant. The E1 transition operator involved in each μ_q ($q=+1,-1,0$) is expressed as $\sqrt{4\pi/3}\; rY_{1q}(\mathbf{r})$, with the z axis is taken along the magnetization direction. Equations (1) and (2) are sum rules regarding the XMCD spectra, while (3) is for XAS with unpolarized light. In the spin sum rule, Eq. (2), we omit for simplicity the contribution from the spin magnetic dipole[16]. It is important to note that a further assumption – final states are classified into pure $j_+(2p_{3/2})$ and $j_-(2p_{1/2})$ excitations and the L_3 and L_2 edges are well separated in energy – is involved in Eq. (2); the XMCD spectrum has to be integrated separately at each edge. The common proportionality constant κ, which is experimentally unknown, is given by a dipole radial matrix element squared

$$\kappa = \langle R_{2p}|r|R_{3d}\rangle^2. \tag{4}$$

By dividing (1) and (2) by (3), the constant κ is eliminated from the expressions:

$$\frac{\int(\mu_+ - \mu_-)d\omega}{\int(\mu_+ + \mu_- + \mu_0)d\omega} = \frac{1}{2}\frac{m_{\rm orb}}{n_{\rm h}}, \tag{5}$$

$$\frac{\int_{j_+}(\mu_+ - \mu_-)d\omega - 2\int_{j_-}(\mu_+ - \mu_-)d\omega}{\int(\mu_+ + \mu_- + \mu_0)d\omega} = \frac{1}{3}\frac{m_{\rm spin}}{n_{\rm h}} \tag{6}$$

which can be used to evaluate the individual $m_{\rm orb}$ and $m_{\rm spin}$ (per hole). On the other hand, the ratio of $m_{\rm orb}$ to $m_{\rm spin}$ is found from the XMCD spectrum alone. Eq. (1) divided by (2) yields

$$\frac{\int(\mu_+ - \mu_-)d\omega}{\int_{j_+}(\mu_+ - \mu_-)d\omega - 2\int_{j_-}(\mu_+ - \mu_-)d\omega} = \frac{3}{2}\frac{m_{\rm orb}}{m_{\rm spin}} \tag{7}$$

and contains neither κ nor $n_{\rm h}$.

The derivations of the sum rules explicitly assume that the Cr $3d$ orbitals will contribute a total of 10 electrons to the (occupied and unoccupied) bands, and that κ provides the normalization needed to relate experiments and theory. Equation (4) dictates that the XAS/XMCD measurement employs a localized atomic function rR_{2p} in probing the Cr $3d$ states. The difficulty is in defining the normalized $3d$ functions R_{3d}. To avoid this issue, we propose to calculate the matrix elements coupling the $2p$ core levels and the valance states ψ_i, similar to those that actually occur in the Fermi golden rule

$$\langle rR_{2p}Y_{2,m}\chi_\sigma|\psi_i\rangle \equiv \langle rR_{2p};m,\sigma|\psi_i>, \tag{8}$$

where the projection onto the spherical harmonics $Y_{\ell m}$ and spinor χ_σ takes into account the dipole selection rules, i.e., including the product of the core function and the E1 operator. In the case that ψ_i depends only on atomic-like Cr $3d$ orbitals, then (the square of) these matrix elements are simply κ as defined in Eq. (4). These matrix elements, which are effectively projections of the Cr $3d$ states onto the $2p$ cores, are well-defined since the region of integration is naturally limited by the spatial extent of the localized $2p$ core state, and are determined by the (ℓ=2) partial wave expansion of the valence wave functions, which are also well defined. (The radial function R_{2p} corresponds to the $p_{1/2}$ or $p_{3/2}$ states as appropriate.)

To proceed, we first define a density matrix constructed from bands ψ_i below an energy E

$$\rho(E) = \sum_i \theta(E-E_i)|\psi_i\rangle\langle\psi_i|, \tag{9}$$

and a weighted density matrix

$$\tilde{n}_{m\sigma,m'\sigma'}(E) = \langle rR_{2p};m,\sigma|\rho(E)|rR_{2p};m',\sigma'\rangle, \tag{10}$$

which includes the matrix elements, Eq. (8). The trace of this density matrix gives the effective number, $\tilde{n}(E)$, of $3d$ electrons below an energy E, and is simply related to the nominal number of $3d$ electrons, $n^{(3d)}(E)$, by

$$\tilde{n}(E) = \tilde{\kappa}\, n^{(3d)}(E). \tag{11}$$

Again, if the simplified assumptions regarding R_{3d} are satisfied, then κ and $\tilde{\kappa}$ would be equivalent.

The final step is to provide a normalization of $\tilde{\kappa}$. There exists an energy $E_{\rm c}$ ($> E_F$) that separates the $3d$ and $4d$ manifolds; this energy can be determined by inspecting the local density of states and the nodal structure of the radial wave functions (i.e., the $4d$ radial functions have an additional radial node). By imposing the condition that the $3d$ states contribute 10 electrons, $n^{(3d)}(E_{\rm c})$=10, we arrive at the following formula for the $3d$ density matrix expressed solely in terms of $\tilde{n}$ and thus is readily calculated from the DFT orbitals,

$$n^{(3d)}(E_F) = \frac{10}{\tilde{n}(E_{\rm c})}\tilde{n}(E_F). \tag{12}$$

The present DFT method to calculate $3d$ moments from Eq. (12) is more in line with the XAS/XMCD experiment

than other computational schemes (e.g., the use of certain integration range for $\mathbf{A}(\mathbf{r})$ or use of maximally localized Wannier functions[21]); both the experiment and the present theory rely on the localized radial function rR_{2p} to extract the $3d$ contributions. Therefore, the ground-state $m_{\rm spin}$ and $m_{\rm orb}$ calculated using the present theory should represent the experiments well as long as the sum rule application on the experimental side is not deteriorated due to background removal errors and/or final-state j-j mixing.

III. EXPERIMENTAL PROCEDURES

Micron-size crystals typically 10×10×1 μm^3 were cut from a bulk single crystal $CrNb_3S_6$ by using an FIB technique, and the thickness of the center was reduced down to approximately 100 nm[22]. These were mounted on a Ta substrate with a 5 μm diameter pinhole using W, as shown in Fig. 2. Since the Ta does not allow the x-rays to pass, we obtain magnetic information only for the thin part of the sample.

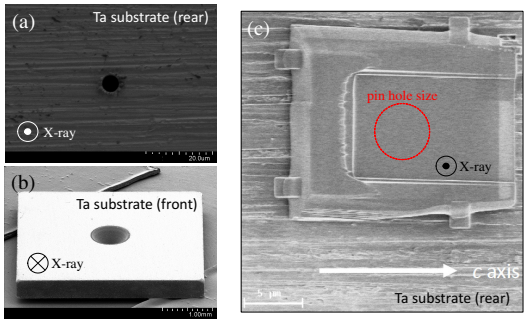

FIG. 2: (Color online) (a, b) Ta substrate (rear and front panel) and (c) micro-processed $CrNb_3S_6$ thin specimen mounted in the rear panel of Ta substrate. In (c), the pin hole size with the 5 μm diameter is displayed.

The XAS/XMCD spectroscopy was carried out using beam line BL25SU of SPring-8[23]. The photoabsorption spectra were obtained by directly measuring the intensity of the transmitted light. The Ta substrate with micro-processed specimen was placed on the sample holder specificated to the XMCD platform in contact with indium foil to maintain sufficient thermal conductivity. The measurements were performed at 10 K, which is sufficiently lower than $T_{\rm c} \sim 130$ K. The magnetic field H of ±4 kOe, which by far exceeds $H_{\rm c} \sim 2$ kOe, was applied perpendicularly to the chiral axis (c-axis) to realize a forced FM state with in-plane magnetization. The x-ray beam was almost parallel to H. In order to minimize possible artifacts caused by the asymmetry of experimental setups, we took an average of the spectra measured at $H = \pm$ 4 kOe; $\mu(+) = \{\mu(\sigma_+, +H) + \mu(\sigma_-, -H)\}/2$ and $\mu(-) = \{\mu(\sigma_-, +H) + \mu(\sigma_+, -H)\}/2$ were employed in the present study. Note that $\mu(+)$ and $\mu(-)$ are the spectra with photon spin parallel and antiparallel to the magnetic field, respectively. In applying the sum rules, we define the following four integrals:

$$\int (\mu(+) - \mu(-))d\omega = A, \quad (13)$$

$$\int (\mu(+) + \mu(-))d\omega = B, \quad (14)$$

$$\int_{j_+} (\mu(+) - \mu(-))d\omega = C, \quad (15)$$

$$\int_{j_-} (\mu(+) - \mu(-))d\omega = D, \quad (16)$$

where $A = C + D$. Approximating the integral of unpolarized XAS, $\int(\mu_+ + \mu_- + \mu_0)d\omega \simeq \frac{3}{2}\int(\mu_+ + \mu_-)d\omega = \frac{3}{2}B$, we rewrite Eqs. (5)-(7) as

$$A/(\frac{3}{2}B) = \frac{1}{2}\frac{m_{\rm orb}}{n_{\rm h}}, \quad (17)$$

$$(C - 2D)/(\frac{3}{2}B) = \frac{1}{3}\frac{m_{\rm spin}}{n_{\rm h}}, \quad (18)$$

$$A/(C - 2D) = \frac{3}{2}\frac{m_{\rm orb}}{m_{\rm spin}}. \quad (19)$$

In the next section, the values of A to D are estimated and given in Table II.

The DFT calculations were performed assuming ferromagnetic spin configuration with the crystal structure[11] determined experimentally at ambient pressure (summarized in Table I). The all-electron full-potential linearized augmented plane wave (FLAPW) method[24] as implemented in the HiLAPW code was used. The muffin-tin sphere radius was set to 1.1 Å for all atoms. The plane wave cutoffs were 16 and 200 Ry for the wave function and potential, respectively. The Perdew, Burke, and Ernzerhof form of the generalized gradient approximation (GGA)[25] was used for exchange correlation. The Brillouin zone was sampled with a 20×20×20 k-point mesh. The SOC was handled in two different ways: included in each self-consistent cycle or only in the last cycle. Both results were practically identical with regard to the magnetic moments and the MCA energy. The radial function R_{2p} needed to calculate the Cr $3d$ quantities was obtained from a scalar-relativistic calculation of Cr $2p$ core state (i.e., no difference between $2p_{3/2}$ and $2p_{1/2}$) under a spherical and spin-averaged part of the self-consistent potential.

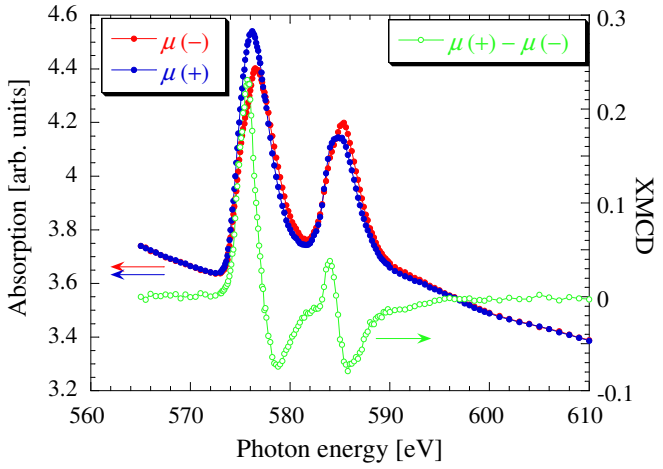

FIG. 3: (Color online) Polarized XAS spectra of $CrNb_3S_6$ at 10 K for $H = \pm 4$ kOe. $\mu(+)$ and $\mu(-)$ represent the XAS with the photon spin parallel and antiparallel to the external magnetic field, respectively. The MCD spectrum is defined as $\mu(+) - \mu(-)$. The Cr L_3 and L_2 edges produce XAS peaks around 577 and 585 eV, respectively.

IV. XMCD RESULTS

Figure 3 shows the XAS spectra $\mu(+)$ and $\mu(-)$ measured at 10 K, which are characterized by two-peak structure embedded in a broad almost linear background with a negative slope. The peaks located around 577 and 585 eV are assigned to the Cr L_3 and L_2 edges, respectively. For photon energies from 572 to 596 eV, the XMCD spectrum defined as $\mu(+)-\mu(-)$ shows characteristic signals. The spectrum exhibits a dispersive lineshape at each of the L_3 and L_2 edges: it starts with a sharp positive peak followed by a negative hump. In the L_3 region, the positive signals prevail over the negative ones. By contrast, for the L_2 edge, the negative signals in the hump dominate over the positive signals of the precursor peak. The alternating sign of the dominant XMCD signals from positive (at the L_3 edge) to negative (L_2) is consistent (based on the transition probability from the $2p$ core state to the empty states in the $3d$ shell) with the fact that the positive $m_{\rm spin}$ (negative spin angular momentum) is induced in the $3d$ shell in the ground state. (See Ref.[26] and Appendix A.) Note that the positive peak in the L_2 region is much weakened compared to that in the L_3 edge and overlaps with the L_3 negative hump.

Figure 4(a) shows the photon energy dependence of $\mu(+) + \mu(-)$. It has a background, which is constructed with the combination of two linear-like terms and two arctangent functions. As explained below, reasonable consideration of background contributions enables us to estimate B, so that we can estimate the denominator in the sum rules Eqs. (17) and (18), i.e., $\frac{3}{2}B$. At first, we assume an almost linear background contribution (black line in Fig. 4(a)), termed bkg.(1), so that the residual spectra for < 568 eV and > 592 eV have constant values as shown with the green data in Figs. 4(a) and 4(b). Next, we consider a background component, termed bkg.(2), consisting of two arctangent functions centered at the edge jumps, as shown with purple data in Fig. 4(b). The ratio of arctangent background for L_3 and that for L_2 is assumed to be 5:3, so that it becomes consistent with the intensity ratio of intrinsic L_3 and L_2 photoabsorption (1.6:1.0). Removing all the background, the residual spectra termed Y is shown in Fig. 4(b) by the dark-green color. Its integral with respect to the energy, shown with light-red in Fig. 4(b), yields B∼10.514.

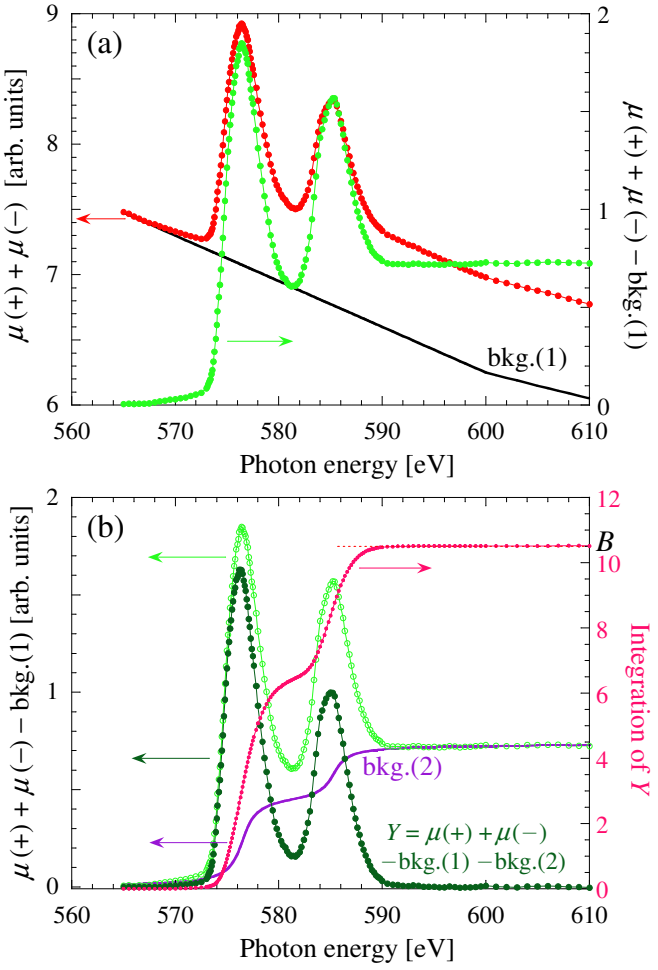

FIG. 4: (Color online) (a) The spectra of $\mu(+) + \mu(-)$. Also shown, the spectra of $\mu(+) + \mu(-)$ after subtracting linear-like background components bkg.(1). (b) Consideration of arctangent background components, bkg.(2), for the spectrum of $\mu(+) + \mu(-)$ and the integration of the residual spectrum Y ($= \mu(+) + \mu(-)$ − bkg.(1) − bkg.(2)) with respect to the energy. The ratio of arctangent background for L_3 and L_2 became approximately 5:3, consistent with the ratio (1.6:1.0) of the Y intensity for L_3 and that for L_2. The full width at half maximum for Y of L_3 is almost the same as that for Y of L_2; there is a minimum of their overlap at 581.3 eV. The integration value of Y corresponds to B in Eq. (14).

For the next step, we consider the calculation of the numerator of Eq. (17). Figure 5 shows the XMCD spectrum and its integral with respect to the photon energy. In the case of estimating small integration value, the scatter in the data may result in indispensable estimation error. Thus, after smoothing the XMCD data for < 572 eV and > 596 eV, we integrated them against the energy to estimate A in Eq. (13). We evaluated A to be -0.031102 (Table II), and obtained $m_{\rm orb}/n_{\rm h} = 2A/(\frac{3}{2}B) = -3.944 \times 10^{-3}$. The errors in estimating A and B are estimated to be $\pm 10\%$ (by varying the smoothing range) and $\pm 7\%$ (by varying the background contribution), respectively, so that $m_{\rm orb}/n_{\rm h}$ has the error of $\pm 12\%$.

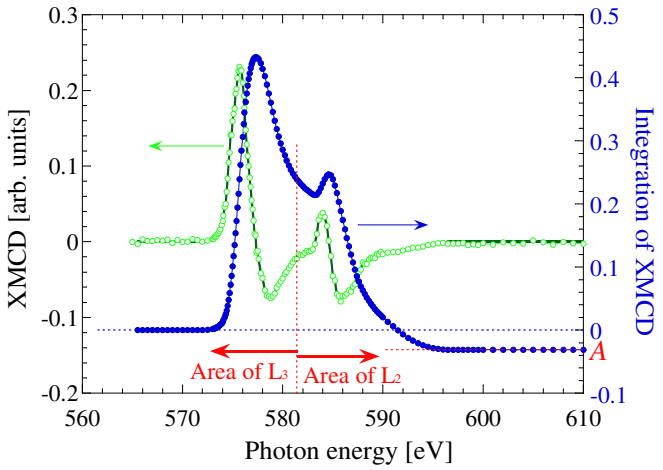

FIG. 5: (Color online) XMCD spectrum $\mu(+) - \mu(-)$ and its integral with respect to the energy. The border between the L_3 and L_2 regions, 581.3 eV, determined from the XAS minimum in Fig. 4(b), is shown.

Third, we attempt to estimate two integral values of the XMCD, C and D appearing in Eq. (18). As we have seen in Fig. 3, the XMCD spectrum consists of two dispersive structures, one in the lower energy side (L_3) and the other higher energy side (L_2). Although the two structures are overlapping, we propose a tentative border between the L_3 area and the L_2 one at 581.3 eV in Fig. 4(b), and do the integration of XMCD for both lower and higher energy sides. Consequently we obtain $C = 0.24167$ (Eq. (15)) and $D = -0.27277$ (Eq. (16)), resulting in $m_{\rm spin}/n_{\rm h} = 1.498\times10^{-1}$ according to Eq. (18). If we adopt $n_{\rm h} = 7$, based on the nominal valency of Cr^{3+} and the magnetization measurements[6] and considered to be an upper bound of $n_{\rm h}$, we obtain $m_{\rm orb} = -2.761\times10^{-2}$ $\mu_{\rm B}$, and $m_{\rm spin} = 1.048$ $\mu_{\rm B}$, as shown in Table III. Note that the estimated $m_{\rm spin}$ is far smaller than the expected value of 3 $\mu_{\rm B}$. Even if the L_3-L_2 boundary is shifted toward the lower energy side, for instance 580.3 eV, there is only a small increase in $m_{\rm spin}/n_{\rm h}$ to 1.676×10^{-1} ($C = 0.27292$ and $D = -0.30402$), and $m_{\rm spin}$ for $n_{\rm h}$=7 increases just to 1.173.

TABLE II: Sum rule based estimations of A, B, C, and D.

A	B	C	D
-0.031102	10.514	0.24167	-0.27277

TABLE III: Sum rule based estimations of $m_{\rm orb}$ and $m_{\rm spin}$ in unit of $\mu_{\rm B}$ based on nominal $n_{\rm h} = 7$ and theoretically predicted $n_{\rm h} = 5.84$.

	$n_{\rm h} = 7$	$n_{\rm h} = 5.84$
$m_{\rm orb}$	-2.761×10^{-2}	-2.303×10^{-2}
$m_{\rm spin}$	1.048	8.745×10^{-1}
$m_{\rm spin}{}'$ ($SC = 1.4$)	1.467	1.224
$m_{\rm orb}/3$	-9.203×10^{-3}	-7.677×10^{-3}

According to Goering's sum rule correction, the mixing factor X is estimated from the intensity ratio r_{23} of L_2 to L_3 as $X = (2r_{23}\text{-}1)/(r_{23}\text{+}1)$[18] and the spin correction factor (SC) is obtained as $SC = 1/(1-2X)$. For instance, $SC = 3$ requires $X = 1/3$ and $r_{23} = 0.8$. In the present XMCD experiments, we derive $r_{23} = 0.62$, $X = 0.15$, and $SC = 1.4$. From these, we obtain 1.467 for the calibrated $m_{\rm spin}$ value ($m_{\rm spin}{}'$) as shown in Table III, a value approximately half of the 3 $\mu_{\rm B}$ observed in the bulk magnetization measurements[6,12]. The X depends on how an *arctan* step background is estimated, whereas it is now impossible to derive $r_{23} = 0.8$. Thus, in the present case, we conclude that the spin sum rule is useless.

V. DFT RESULTS

In this section, ground-state DFT calculations are presented to support the previous discussion of the Cr local moments based on the XMCD measurement, and furthermore, to understand the role of the individual atomic SOC in the forced FM state.

In subsection V A, in order to capture the fundamental aspects of the electronic structure of $CrNb_3S_6$, we first perform a spin-polarized scalar-relativistic calculation (without SOC) where the results do not depend on the magnetization direction. In particular, we focus on the hybridization of Cr 3*d* orbitals. In V B, with SOC included, the easy-plane type MCA and Cr 3*d* magnetic moments are discussed in detail. In V C, the individual roles of Cr and Nb SOC are analyzed.

A. Electronic structure

Figure 6 shows the total density of states (DOS) calculated without SOC, which agrees well with those reported previously[12,27,28]. (We use the convention that spin up (down) denotes the majority (minority) spin.) S 3*p* and Nb 4*d* states are located mainly in the energy intervals

[−8:−2] and [−2:5] eV, respectively. Cr l=2 states (highlighted by red) show large exchange splitting: most of the spin-down states are pushed above E_F. Both spin channels are metallic with a finite DOS at E_F. Farther above E_F, a broad continuum feature starts from 5 eV in the DOS of both spins, indicating that the 3d region ends at 5 eV. Indeed, above this energy, Cr l=2 partial waves become 4d-like, picking up an additional radial node. We set E_c=5 eV in the analysis of the Cr 3d shell using Eq. (12) discussed later.

Figure 7 shows partial d-wave DOS projected onto Nb hexagonal harmonics and Cr e'_g, a_{1g}, and e_g harmonics (see Appendix B for the complete definition of these orbitals). The top two panels are for the Nb(2a) and (4f) sites while the bottom two are for Cr. We begin with the spin-up states shown in the left panels, Fig. 7(a). The e'_g states (the left lowest panel) form a sharp peak well below E_F in a narrow energy window (from −2 to −1 eV) that appears to be consistent with the localized $t_{2g\uparrow}$ scheme. On the other hand, the rest of the t_{2g} manifold – the a_{1g} state (red highlighted in the second lowest panel) – is delocalized to a remarkable extent, spread over a wide energy range, even extending across E_F to the unoccupied levels, and with a similar bandwidth to the delocalized e_g state that hybridizes well with S 3p orbitals. This unexpected a_{1g} delocalization is a consequence of strong hybridization with Nb 4d orbitals. A clear indication of strong mixing is seen in the second panel: Nb(4f) z^2 (red highlighted) has peak structures resonating with a_{1g}.

Regarding the spin-down bands, Fig. 7(b), the occupied states from −2 eV and above are mainly Nb z^2 and x^2-y^2/xy orbitals. Although the exchange splitting pushes most of the spin-down Cr 3d states above E_F, some of them come into the occupied levels and show a broader energy spectrum. They form chemical bonds with Nb and S orbitals and are (together with the spin-up 3d states of the same character) magnetically dead. The states just at E_F are exclusively of Nb z^2 character. The unoccupied body of spin-down states, starting from 0.2 eV, is composed of all d orbitals from Nb and Cr.

The method described in Eq. (12) – defining the Cr 3d quantities as probed by the Cr 2p core – is applied to the present non-SOC electronic structure. Table IV summarizes the Cr 3d occupation numbers obtained. The spin-up and -down 3d states are about 3.6 and 0.6 electrons, respectively, yielding a total 3d electron number of 4.16 (n_h=5.84) and a 3d spin magnetic moment m_{spin}=3.01 μ_B. Roughly speaking, there are 0.6 magnetically dead electrons in each spin; the magnetically active part exhibits an electron configuration $(e'_g)^{1.8}(a_{1g})^{0.8}(e_g)^{0.5}$ for spin up, in sharp contrast to the localized picture with $(t_{2g\uparrow})^3$. The occupation number for $a_{1g\uparrow}$ deviates from unity with some of $e_{g\uparrow}$ states being occupied. Both $a_{1g\uparrow}$ and $e_{g\uparrow}$ states show up at E_F and contribute to the conductivity in the spin-up channel. Their metallic conduction may account for the relatively high T_c despite the rather long Cr-Cr interatomic distance.

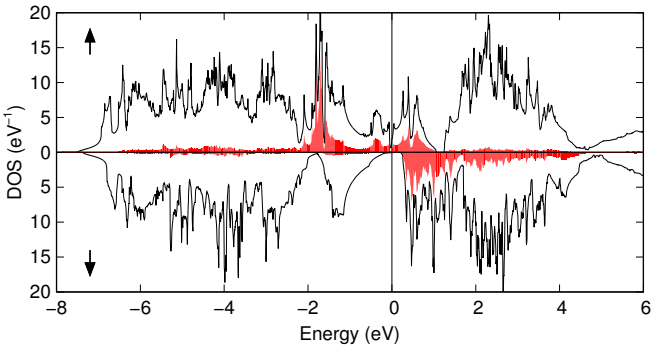

FIG. 6: Spin-up (upper panel) and -down (lower) density of states. Contributions from Cr valence l=2 states (within the muffin-tin sphere) are highlighted by red. Energy zero refers to the Fermi level.

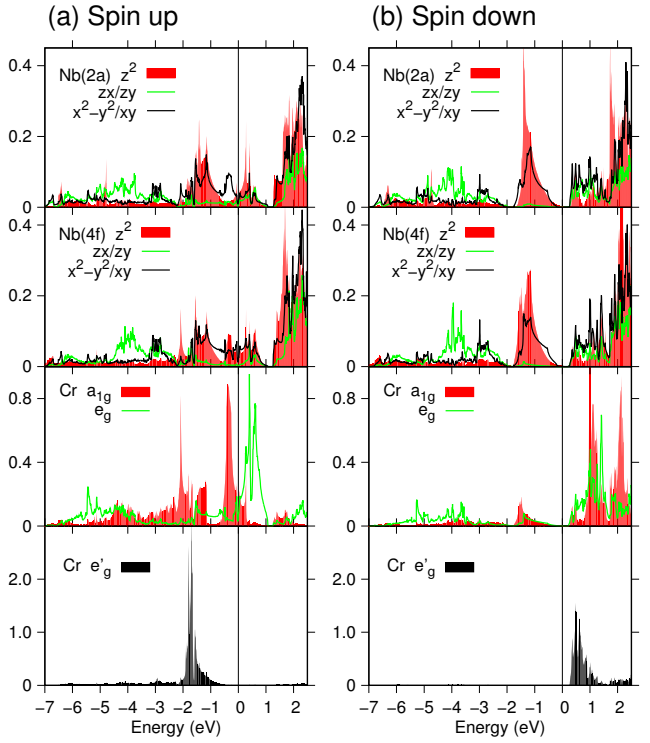

FIG. 7: Partial d-wave density of states (in unit of eV^{-1}) projected onto Nb hexagonal harmonics and Cr e'_g, a_{1g}, and e_g harmonics within the muffin-tin spheres for (a) spin up and (b) spin down. Multiplicity of atoms and orbitals is excluded. Note that the vertical scale is different in each panel.

B. MCA and magnetic moment

Turning SOC on, we examine the MCA to see whether DFT reproduces the easy-plane type anisotropy. The total energy variation as a function of magnetization direction $E(\theta,\phi)$ is calculated using the force theorem[29]. Figure 8 shows $\Delta E(\theta) = E(\theta) - E(0)$ as a function of the polar angle θ (the azimuth ϕ dependency is negligi-

TABLE IV: Cr $3d$ occupation numbers calculated from the $3d$ density matrix defined in Eq. (12).

Spin	e_g'	a_{1g}	e_g	Sum
up	1.88	0.89	0.82	3.59
down	0.08	0.13	0.36	0.58
up − down	1.80	0.76	0.45	3.01

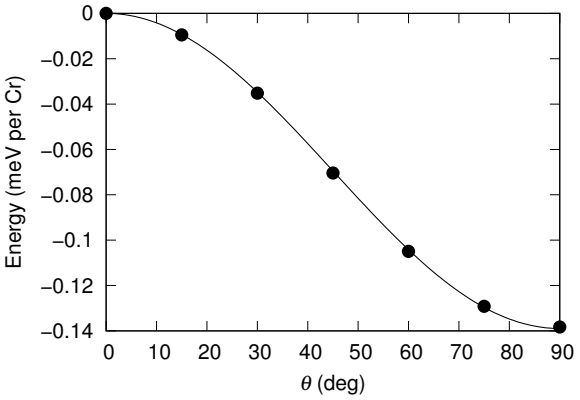

FIG. 8: Total energy variation as a function of magnetization direction. θ=0 (90) degree corresponds to magnetization direction parallel (perpendicular) to the c axis. Dots represent the DFT energies while solid line shows a $\sin^2\theta$ fit.

bly small). The easy-plane type anisotropy is correctly reproduced with an energy minimum located at θ=90°. The energy variation follows a $\sin^2\theta$ behavior (solid line), indicating that the MCA is dominated by the second order effect of the SOC. The MCA energy, the energy difference between the hard-axis and easy-plane magnetizations, is found to be 0.14 meV per $CrNb_3S_6$ unit, in a good agreement with the ESR experiment[14] and previous DFT calculations[28].

The spin magnetic moment with SOC turned on remains the same as that in the non-SOC case, and thus shows no dependence on the choice of magnetization direction. The total spin magnetic moment (obtained by integrating the spin density over the whole space) is 3.004 μ_B per $CrNb_3S_6$, again consistent with the previous DFT result[28]. The contributions in each muffin-tin sphere are 2.500, 0.055, 0.003, and 0.005 μ_B, from Cr, Nb($2a$), Nb($4f$), and S, respectively; a small positive spin moment is induced at the Nb($2a$) site while the moments at the Nb($4f$) and S sites are negligible. Figure 9 shows a two-dimensional spin density map on a hexagonal $(11\bar{2}0)$ plane where Cr and Nb atoms are found. The spin density is peaked around Cr and extends with positive sign to a radius ∼1.8 Å. The Nb($4f$) site (sitting above and below Cr along c) has sizable spin density distribution with alternating signs even though it is integrated out to be nearly zero; in particular, a negative distribution along the c axis is clearly seen, which is a signature of

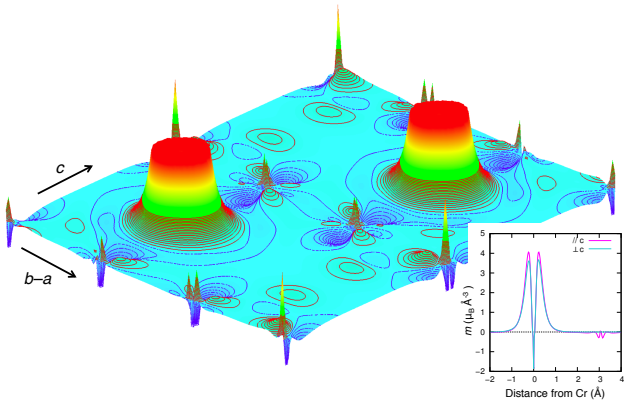

FIG. 9: Spin magnetization density mapped on a hexagonal $(11\bar{2}0)$ plane. The high density around the Cr is cut off, and the low density region (< 0.1 μ_B Å^{-3}) is highlighted by contour lines – red (blue) lines are for small positive (negative) densities. Inset: one-dimensional plots of the spin magnetization density parallel and perpendicular to the c axis, on the $(11\bar{2}0)$ plane through Cr nucleus.

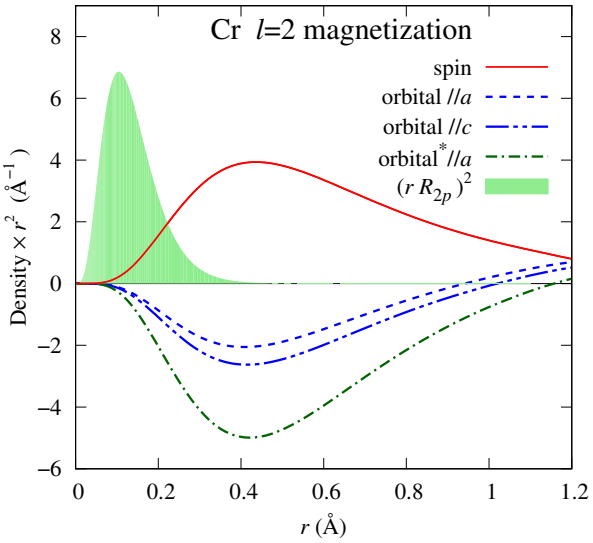

FIG. 10: Spin and orbital magnetization densities originating from the Cr l=2 partial wave. The spherical part of the density is multiplied by the weighting factor r^2. The orbital contributions are magnified by 100 relative to the spin, and are shown for magnetization along the a and c axes. The dash-dotted line ('orbital*') is obtained for the Cr-only SOC calculation (see Sec. V C for detail). The radial density of the Cr $2p$ core radial function R_{2p} is also shown.

the Cr a_{1g}-Nb z^2 interaction.

Now we shift our focus to the Cr l=2 partial wave. Spin and orbital magnetization densities are shown in Fig. 10. The spin density is positive and has a large tail, well beyond the muffin-tin radius of 1.1 Å; the orbital density (displayed with multiplying a factor of 100) is

TABLE V: Cr 3d electron number, spin and orbital magnetic moments (μ_B), and spin magnetic dipole calculated for two magnetization directions: a (easy axis) and c (hard axis). For the top two entries ("R_{2p}") the Cr 2p core is used as a local probe, Eq. (12). The errors are estimated to be ±0.4% for each quantity listed, determined by shifting the boundary energy E_c by ±0.5 eV. The bottom two lines ("MT") are calculated simply by integrating the l=2 partial wave within the Cr muffin-tin sphere.

Direction α	N	m_{spin}	$m_{orb}\times10^3$	$7\langle T_\alpha\rangle$
R_{2p}: a	4.16	3.01	−16.3	−0.156
c	4.16	3.01	−20.1	0.308
MT: a	3.74	2.47	−9.4	−0.144
c	3.74	2.47	−13.3	0.286

predominately negative until turning positive at $r \sim 1$ Å. It is apparent that the spin and orbital moments are coupled antiparallel, as expected from an atomic picture for the less-than-half filled case. However, the quantitative values of the 3d magnetic moments depend on the choice of integration region because of the tails in their density distributions. Furthermore, the l=2 partial wave (which is used in calculating the density distribution in Fig. 10) is not a pure Cr 3d wave; at large r it includes orbital tails from the surrounding atoms. The Cr 2p core function R_{2p} (shown by pale green in Fig. 10), however, is localized in region close to the nucleus where the l=2 wave predominately originates from the Cr 3d state. Using rR_{2p} as a probe for Cr 3d state, we calculate local quantities in the 3d shell as summarized in Table V. The Cr 3d spin magnetic moment m_{spin} obtained is nearly 3.0 μ_B, consistent with a proper picture that the Cr 3d state is responsible for the magnetism in $CrNb_3S_6$, and is greatly enhanced from the l=2 muffin-tin value of 2.5 μ_B (Table V). The Cr 3d orbital moment m_{orb} is found to have a negative sign (antiparallel to the spin) with small values of −0.016 μ_B and −0.020 μ_B for the in-plane and out-of-plane magnetization, respectively. These values are enhanced from the l=2 muffin-tin values in Table V, indicating that the sign change of the orbital distribution at $r \sim 1$ Å (seen in Fig. 10) is not from the pure 3d orbital but from hybridization effects that develop positive orbital distribution in the 3d tail region. The ratio between orbital and spin is $m_{orb}/m_{spin}\times100$= −0.54 (in-plane magnetization) and −0.69 (out-of-plane). Naively it is counterintuitive that m_{orb} in the easy-plane magnetization has smaller magnitude than that in the hard-axis magnetization. We will come back to this point in the next subsection. The spin magnetic dipole shown in Table V obeys the relation $\sum_{\alpha=x,y,z}\langle T_\alpha\rangle \sim 0$, which is known to hold in the weak SOC case[30]. Ignoring its contribution in the application of the spin sum rule would degrade the estimated m_{spin} by only 5% for the in-plane magnetization. The Nb and S atoms have very small orbital moments (less than 10^{-3} μ_B for the in-plane magnetization), which we will not discuss further here.

TABLE VI: Comparison between experimental and theoretical m_{orb} values for the in-plane magnetization. The DFT-estimated hole number, n_h = 5.84, is used in the XMCD orbital sum rule. The ratio m_{orb}/m_{spin} assumes m_{spin} = 3.

	m_{spin}	$m_{orb}\times10^3$	m_{orb}/m_{spin}(=3) [%]
theory	3.01	−16.3	−0.54
MCD	–	−23.0	−0.77

TABLE VII: Cr 3d orbital magnetic moment, m_{orb}, calculated by turning the SOC on only at selected element. In unit of 10^{-3} μ_B. Two magnetization directions, along a and c axes, are examined. The Cr 2p local-probe technique is used.

Direction α	Cr	Nb	S
a	−38.9	12.7	9.9
c	−32.0	7.8	3.5

The Cr 3d electron number is calculated to be 4.16 (unchanged from the non-SOC calculation), which gives the number of holes in the 3d shell, n_h=5.84. Using this n_h in the XMCD orbital sum rule, the experimentally deduced m_{orb} is compared with the DFT value in Table VI. A fairly good agreement is achieved between the experiment and theory, especially taking into account the fact that the DFT tends to underestimate m_{orb}. We conclude that the order of m_{orb}/m_{spin} is $\sim -1\%$.

C. Cr and Nb SOC

We have seen that the MCA is of easy-plane type and that the unquenched Cr 3d orbital moment is aligned antiparallel to the spin moment. There is no doubt that the SOC in the Cr 3d shell plays a major role. However, the spin-orbit coupling constant λ for the Nb 4d orbital (0.1 eV) is three times as large as that for Cr 3d orbital (0.034 eV) and thus Nb SOC may also play an important role.

In this section, we examine the individual atomic SOC and analyze in detail the origin of the easy-plane MCA. We turn on the SOC only at selected element(s) and calculate the MCA energy as summarized in Fig. 11(a). Turning on the Cr SOC alone provides 50% of the full MCA energy, indicating that the Cr SOC is indispensable (as expected) but the other elements provide some contributions. However, pure elemental SOCs of Nb and S give very small MCA energies, 13% and 10%, respectively; the full MCA is not reproduced from the simple sum of these individual effects. When the Cr and Nb SOCs are turned on together, 96% of the full MCA is reproduced. This clearly shows that the Nb SOC enhances the MCA, i.e., the Nb and Cr SOC interact constructively.

To further understand this enhancement of the MCA through the Nb SOC, we adopt a second-order perturbation theory. We write the unperturbed eigenstates (in

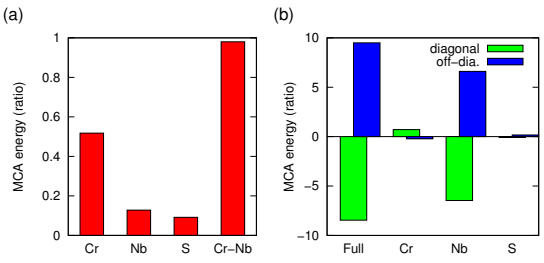

FIG. 11: (a) DFT-calculated MCA energies obtained by selectively turning on SOC for different elements, given as the ratio to the full MCA value (0.14 meV per $CrNb_3S_6$). (b) Same as (a) but decomposed into the spin-diagonal and spin-off-diagonal SOC processes. Note that the vertical scale is different from (a).

the FM state without the SOC) as $\{\epsilon_i, \varphi_i\}$, where i is a combined index of wave vector $\mathbf{k}$, spin σ ($= \pm 1/2$), and band index n. The SOC perturbation depends on the magnetization direction $\hat{\mathbf{m}}$ ($|\hat{\mathbf{m}}| = 1$) and may be written as

$$H'_{\hat{\mathbf{m}}} = H_{\rm SO}(\hat{\mathbf{m}}) = U^{\dagger}_{\hat{\mathbf{m}}} H_{\rm SO} U_{\hat{\mathbf{m}}} \tag{20}$$

with the spin rotation matrix $U_{\hat{\mathbf{m}}}$ (see Appendix C) and with $H_{\rm SO}$ being a sum of atomic SOC Hamiltonian $\lambda \mathbf{L}\cdot\mathbf{s}$ of Cr $3d$, Nb $4d$ and S $3p$ orbitals,

$$H_{\rm SO} = H_{\rm SO}^{\rm (Cr)} + H_{\rm SO}^{\rm (Nb)} + H_{\rm SO}^{\rm (S)}. \tag{21}$$

According to the force theorem[29], the MCA energy is given in terms of the band energy summation over occupied states,

$$E(\hat{\mathbf{m}}) = \sum_i f_i^{(\hat{\mathbf{m}})} \epsilon_i^{(\hat{\mathbf{m}})}, \qquad E_{\rm MCA} = E(\hat{\mathbf{m}} \parallel c) - E(\hat{\mathbf{m}} \perp c)$$

where $f_i^{(\hat{\mathbf{m}})}$ and $\epsilon_i^{(\hat{\mathbf{m}})}$ are the band occupation number and band energy with the perturbation incorporated. Using a second-order perturbation theory and disregarding the change in the band occupation number (that is small in the present case), the band energy sum can be found as

$$E(\hat{\mathbf{m}}) = E_0 + \sum_{i,j} f_i(1-f_j) \frac{|\langle i|H'_{\hat{\mathbf{m}}}|j\rangle|^2}{\epsilon_i - \epsilon_j} \delta_{\mathbf{k}_i \mathbf{k}_j} \tag{22}$$

where only a pair of occupied and unoccupied bands (at the same $\mathbf{k}$) interacting via SOC contributes to the MCA through its $\hat{\mathbf{m}}$ dependence. The relevant matrix element squared is decomposed as

$$|\langle i|H'|j\rangle|^2 = \left|\langle i|H_{\rm SO}^{\rm (Cr)}|j\rangle\right|^2 + \left|\langle i|H_{\rm SO}^{\rm (Nb)}|j\rangle\right|^2 + \langle i|H_{\rm SO}^{\rm (Cr)}|j\rangle\langle j|H_{\rm SO}^{\rm (Nb)}|i\rangle + \text{c.c.} \tag{23}$$

where the $\hat{\mathbf{m}}$ dependence and the sulfur related terms are suppressed for simplicity. In addition to the pure individual contributions (the first and second terms of Eq. (23)), a Cr-Nb *interference* term (the third term) exists as well, which may enhance the MCA effectively only if (i) strong hybridization between Cr $3d$ and Nb $4d$ orbitals is seen in both states i and j and (ii) the phases of two SO matrix elements constructively interfere. The DFT result given in Fig. 11(a) indicates that this Cr-Nb interference term doubles the MCA energy compared to that with the Cr SOC alone.

In Fig. 11(b), we further decompose the MCA into two spin processes: spin-diagonal (bands i and j have the same spin, σ_i=σ_j) and spin-off-diagonal SOC process ($\sigma_i \neq \sigma_j$). In the full SOC calculation (a set of two boxes located in the most left of Fig. 11(b)), two spin processes have fairly large energy (nearly one order of magnitude greater than the net MCA energy) while they compete with each other: the spin-off-diagonal process favors in-plane magnetization; the spin-diagonal process favors out-of-plane magnetization. In the case of the Cr-SOC only calculation, the spin-diagonal process (the interaction in the spin-up channel) dominates and provides the easy-plane anisotropy, where a pair of $a_{1g\uparrow}$ and $e_{g\uparrow}$ states should be most relevant. In the Nb-SOC only case, both spin processes have large values (similar to the full SOC calculation) but they almost cancel with different signs, resulting in the only 13% of the full MCA energy. That two processes have nearly identical magnitude is due to the fact that both spins are found in the occupied Nb $4d$ bands. The interference term, however, picks up bands that have substantial Cr $3d$ - Nb $4d$ mixing in their wave functions. Therefore, the occupied counterpart in the interference process is dominated by spin-up (due to the Cr $3d$ spin polarization). From the MCA decomposition analysis (Fig. 11) and the partial DOS analysis (Fig. 7), together with the matrix representation of $\mathbf{L}$ (Appendix B), the occupied-unoccupied pairs of bands that are highly relevant to the MCA are identified as $a_{1g\uparrow}$ - $e_{g\uparrow}$ (for the pure Cr SOC) and $e_{g\uparrow}$ - $e'_{g\downarrow}$ (for the interference SOC).

The Cr $3d$ orbital moment behaves differently in the site-selective SOC calculations. First-order perturbation theory illustrates that the Cr orbital moment is given by

$$\langle L_\alpha^{\rm (Cr)}\rangle = \sum_{i,j} \frac{f_i(1-f_j)}{\epsilon_i - \epsilon_j} \times \left[\langle i|L_\alpha^{\rm (Cr)}|j\rangle\langle j|H'_\alpha|i\rangle\ \delta_{\sigma_i\sigma_j}\delta_{\mathbf{k}_i\mathbf{k}_j} + \text{c.c.}\right] \tag{24}$$

where α=x, y, z. Note that the right-hand size is linear in H' (sum of atomic SOC) and thus $m_{\rm orb}$ in the full SOC calculation is determined by a simple summation of elemental SOC effects. Table VII lists the values of $3d$ orbital moment in the element-selective SOC calculations. The summation of these values indeed reproduce $m_{\rm orb}$ in the full SOC calculation (Table V). It is interesting to see that in the Cr-only SOC calculation $m_{\rm orb}$ is much larger than its full SOC value and now the in-plane $|m_{\rm orb}|$ is greater than that for the out-of-plane (hard-axis) magnetization. The Nb- and S-only SOC calculations yield

opposite-sign orbital moments in the Cr 3d shell. From these results we conclude that SOC on the Nb and S atoms interfere destructively to decrease the Cr orbital moment.

VI. CONCLUSION

We have performed the XAS/XMCD measurements for $CrNb_3S_6$ with in-plane magnetization at the Cr $L_{2,3}$ edges. The XMCD spectrum, exhibiting dispersive lineshapes for each of the L_3 and L_2 edges, unambiguously reveals that the Cr orbital magnetic moment is not quenched and is coupled antiparallel to the spin counterpart. The magnitude of orbital magnetic moment is estimated to be approximately 0.02 μ_B. The quantitative evaluation of spin magnetic moment via the sum rules is unsuccessful due to the small spin-orbit splitting in the Cr 2p core. These experimental findings on the Cr local magnetism are supported by the DFT calculations, where, analogous to the experiment, the radial part of the Cr 2p core state is employed to define the 3d shell. Theoretical analyses show that the SOC in the Nb 4d orbital, as a consequence of its strong hybridization with the Cr 3d orbital, plays an important role in determining the MCA and the Cr 3d orbital moment.

Acknowledgments

This work was supported by Grants-in-Aid for Scientific Research, Grant No. (S) 25220803, from the Ministry of Education, Culture, Sports, Science and Technology (MEXT), Japan; the Center for Chiral Science in Hiroshima University (the MEXT program for promoting the enhancement of research universities, Japan); JSPS Core-to-Core Program, A. Advanced Research Networks; and the National Science Foundation EFMA-1741673. The synchrotron radiation experiments were performed at the BL25SU in SPring-8 with the approval of the Japan Synchrotron Radiation Research Institute (JASRI) (Proposal No. 2015B1018 and No. 2016A1029).

Appendix A: Transition probability

Imada et al. have tabulated the transition probability in the $p \to d$ photoabsorption when the core hole j is a good quantum number and the d states are labeled by the spin and the orbital magnetic quantum number[26]. Figure 12(a) reproduces their result; Fig. 12(b) is for the case that the d states are labeled by a_{1g}, e'_g, and e_g manifolds (under the D_{3d} crystalline field) with both the magnetic field and the photo propagation being perpendicular to the threefold axis.

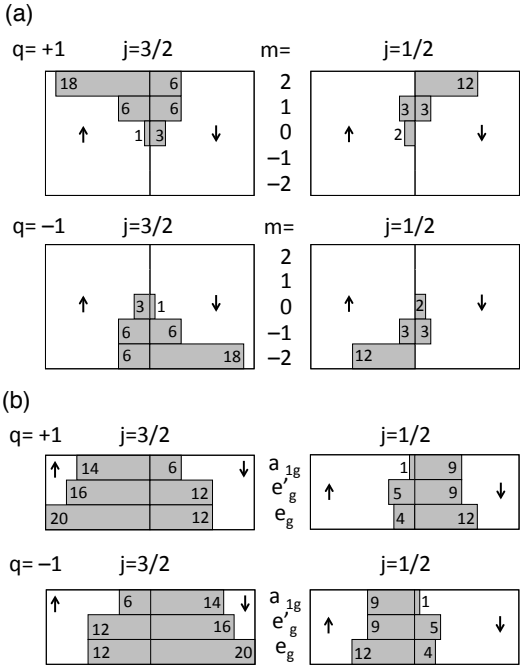

FIG. 12: Distribution of weights of the transition probability to the d states in the $p \to d$ photoabsorption process with the photon spin $q = \pm 1$ when the core hole j is a good quantum number. (a) d states labeled by the orbital magnetic quantum number m (after Ref.[26]). (b) d states under the D_{3d} crystalline field. The magnetization and the photo propagation directions are perpendicular to the threefold (z) axis.

Appendix B: d orbital

The hexagonal harmonics $(z^2, zx, zy, x^2 - y^2, xy)$ defined in the coordinate system (x, y, z) in Fig. 1(b) are considered the natural basis functions for Nb 4d states. In this basis set, the orbital angular momentum operator is given in the matrix representation

$$L_x = \begin{pmatrix} 0 & 0 & \sqrt{3}i & 0 & 0 \\ 0 & 0 & 0 & 0 & i \\ -\sqrt{3}i & 0 & 0 & -i & 0 \\ 0 & 0 & i & 0 & 0 \\ 0 & -i & 0 & 0 & 0 \end{pmatrix},$$

$$L_y = \begin{pmatrix} 0 & -\sqrt{3}i & 0 & 0 & 0 \\ \sqrt{3}i & 0 & 0 & -i & 0 \\ 0 & 0 & 0 & 0 & -i \\ 0 & i & 0 & 0 & 0 \\ 0 & 0 & i & 0 & 0 \end{pmatrix},$$

$$L_z = \begin{pmatrix} 0 & 0 & 0 & 0 & 0 \\ 0 & 0 & -i & 0 & 0 \\ 0 & i & 0 & 0 & 0 \\ 0 & 0 & 0 & 0 & -2i \\ 0 & 0 & 0 & 2i & 0 \end{pmatrix}.$$

In the main text, Cr $3d$ states are discussed in terms of a_{1g}, e'_g, and e_g manifold (which is valid under D_{3d} symmetry). The trigonal basis functions, x_0 (for a_{1g}), $x_\pm$ (for e'_g), $u_\pm$ (for e_g) are given as follows

$$\begin{aligned} x_0 &= Y_{20}, \\ x_+ &= -\sqrt{\frac{2}{3}}Y_{2-2} - \sqrt{\frac{1}{3}}Y_{21}, \\ x_- &= \sqrt{\frac{2}{3}}Y_{22} - \sqrt{\frac{1}{3}}Y_{2-1}, \\ u_+ &= -\sqrt{\frac{1}{3}}Y_{2-2} + \sqrt{\frac{2}{3}}Y_{21}, \\ u_- &= \sqrt{\frac{1}{3}}Y_{22} + \sqrt{\frac{2}{3}}Y_{2-1} \end{aligned}$$

where the spherical harmonics are defined in the coordinate system (x, y, z) in Fig. 1(b). The orbital angular momentum operator is written in the matrix form with the basis $(x_0, x_+, x_-, u_+, u_-)$,

$$L_x = \begin{pmatrix} 0 & -1/\sqrt{2} & -1/\sqrt{2} & 1 & 1 \\ -1/\sqrt{2} & 0 & 0 & 0 & -1 \\ -1/\sqrt{2} & 0 & 0 & 1 & 0 \\ 1 & 0 & 1 & 0 & 0 \\ 1 & -1 & 0 & 0 & 0 \end{pmatrix}$$

$$L_y = \begin{pmatrix} 0 & -i/\sqrt{2} & i/\sqrt{2} & i & -i \\ i/\sqrt{2} & 0 & 0 & 0 & -i \\ -i/\sqrt{2} & 0 & 0 & -i & 0 \\ -i & 0 & i & 0 & 0 \\ i & i & 0 & 0 & 0 \end{pmatrix},$$

$$L_z = \begin{pmatrix} 0 & 0 & 0 & 0 & 0 \\ 0 & -1 & 0 & -\sqrt{2} & 0 \\ 0 & 0 & 1 & 0 & \sqrt{2} \\ 0 & -\sqrt{2} & 0 & 0 & 0 \\ 0 & 0 & \sqrt{2} & 0 & 0 \end{pmatrix}.$$

Appendix C: SOC Hamiltonian

We write the atomic SOC Hamiltonian as

$$H_{\rm SO} = \lambda \mathbf{L}\cdot\mathbf{s} = \frac{\lambda}{2}\begin{pmatrix} L_z & L_x - iL_y \\ L_x + iL_y & -L_z \end{pmatrix}$$

for the spin basis functions (up and down) defined along the crystalline z axis. The SOC Hamiltonian with the spin quantization axis along an arbitrary direction $\hat{\mathbf{m}}$ (with polar angle θ and azimuthal angle ϕ) is found in the following, by using the spin rotation matrix $U_{\hat{\mathbf{m}}}$[31],

$$H_{\rm SO}(\hat{\mathbf{m}}) = U^\dagger_{\hat{\mathbf{m}}} H_{\rm SO} U_{\hat{\mathbf{m}}} = \frac{\lambda}{2}\begin{pmatrix} \mathbf{L}\cdot\hat{\mathbf{m}} & \mathbf{L}\cdot\tilde{\mathbf{e}} \\ \mathbf{L}\cdot\tilde{\mathbf{e}}^* & -\mathbf{L}\cdot\hat{\mathbf{m}} \end{pmatrix},$$

and

$$\begin{aligned} \hat{\mathbf{m}} &= (\sin\theta\cos\phi,\ \sin\theta\sin\phi,\ \cos\theta)^T, \\ \tilde{\mathbf{e}} &= (\cos\theta\cos\phi + i\sin\phi, \cos\theta\sin\phi - i\cos\phi, -\sin\theta)^T \end{aligned}$$

where $\hat{\mathbf{m}}$ is the directional cosine of the spin quantization axis, and $\tilde{\mathbf{e}}$ is a complex vector ($|\tilde{\mathbf{e}}|^2$=2) orthogonal to $\hat{\mathbf{m}}$. For [001], [100], and [010] directions, the SOC Hamiltonians are

$$\begin{aligned} H_{\rm SO}[001] &= \frac{\lambda}{2}\begin{pmatrix} L_z & L_x - iL_y \\ L_x + iL_y & -L_z \end{pmatrix}, \\ H_{\rm SO}[100] &= \frac{\lambda}{2}\begin{pmatrix} L_x & -iL_y - L_z \\ iL_y - L_z & -L_x \end{pmatrix}, \\ H_{\rm SO}[010] &= \frac{\lambda}{2}\begin{pmatrix} L_y & iL_x - L_z \\ -iL_x - L_z & -L_y \end{pmatrix}. \end{aligned}$$

* Electronic address: mitoh@mns.kyutech.ac.jp
† Electronic address: shishido@uwm.edu

[1] I. E. Dzyaloshinskii, J. Phys. Chem. Solid **4**, 241 (1958).
[2] T. Moriya, Phys. Rev. **120**, 91 (1960).
[3] I. E. Dzyaloshinskii, Sov. Phys. JETP **20**, 665 (1965).
[4] J. Kishine, K. Inoue, and Y. Yoshida, Prog. Theor. Phys., Suppl. **159**, 82 (2005).
[5] Y. Togawa, Y. Kousaka, K. Inoue, and J. Kishine, J. Phys. Soc. Jpn. **85**, 112001 (2016).
[6] T. Miyadai, K. Kikuchi, H. Kondo, S. Sakka, M. Arai, and Y. Ishikawa, J. Phys. Soc. Jpn. **52**, 1394 (1983).
[7] Y. Togawa, Y. Kousaka, S. Nishihara, K. Inoue, J. Akimitsu, A. S. Ovchinnikov, and J. Kishine, Phys. Rev. Lett. **111**, 197204 (2013).
[8] Y. Togawa, T. Koyama, Y. Nishimori, Y. Matsumoto, S. McVitie, D. McGrouther, R. L. Stamps, Y. Kousaka, J. Akimitsu, S. Nishihara, et al., Phys. Rev. B **92**, 220412 (2015).
[9] H. Flack, Helv. Chim. Acta **86**, 905 (2003).
[10] M. Nespolo, Cryst. Res. Techn. **50**, 413 (2015).
[11] M. Mito, T. Tajiri, K. Tsuruta, H. Deguchi, J. Kishine, K. Inoue, Y. Kousaka, Y. Nakao, and J. Akimitsu, J. Appl. Phys. **117**, 183904 (2015).
[12] N. J. Ghimire, M. A. McGuire, D. S. Parker, B. Sipos, S. Tang, J.-Q. Yan, B. C. Sales, and D. Mandrus, Philos. Mag. B **87**, 104403 (2013).
[13] K. Tsuruta, M. Mito, H. Deguchi, J. Kishine, Y. Kousaka, J. Akimitsu, and K. Inoue, Phys. Rev. B **93**, 104402 (2016).
[14] D. Yoshizawa, J. Kishine, Y. Kousaka, Y. Togawa, M. Mito, J. Akimitsu, K. Inoue, and M. Hagiwara, Phys.

Proc. **75**, 926 (2015).
[15] M. Shinozaki, S. Hoshino, Y. Masaki, J. Kishine, and Y. Kato, J. Phys. Soc. Jpn. **85**, 074710 (2016).
[16] P. Carra, B. T. Thole, M. Altarelli, and X. Wang, Phys. Rev. Lett. **70**, 694 (1993).
[17] Y. Teramura, A. Tanaka, and T. Jo, J. Phys. Soc. Jpn. **65**, 1053 (1996).
[18] E. Goering, Philosophical Magazine **85**, 2895 (2005).
[19] S. S. P. Parkin and R. H. Friend, Phys. Rev. B **41**, 65 (1980).
[20] B. T. Thole, P. Carra, F. Sette, and G. van der Laan, Phys. Rev. Lett. **68**, 1943 (1992).
[21] N. Marzari and D. Vanderbilt, Phys. Rev. B **56**, 12847 (1997).
[22] M. Mito, H. Ohsumi, K. Tsuruta, Y. Kotani, T. Nakamura, Y. Togawa, M. Shinozaki, Y. Kato, J. Kishine, J. Ohe, et al., Phys. Rev. B **97**, 024408 (2018).
[23] T. Nakamura, T. Muro, F. Guo, T. Matsushita, T. Wakita, T. Hirono, Y. Takeuchi, and K. Kobayashi, J. Electron. Spectrosc. Relat. Phenom **144-147**, 1035 (2005).
[24] M. Weinert, G. Schneider, R. Podloucky, and J. Redinger, J. Phys.: Condens. Matter **21**, 084201 (2009).
[25] J. P. Perdew, K. Burke, and M. Ernzerhof, Phys. Rev. Lett. **77**, 3865 (1996).
[26] S. Imada, S. Suga, and T. Miyahara, BUTSURI **55**, 20 (2000), (in Japanese; Physical Society of Japan).
[27] A. C. Bornstein, B. J. Chapman, N. J. Ghimire, D. G. Mandrus, D. S. Parker, and M. Lee, Phys. Rev. B **91**, 184401 (2015).
[28] S. Mankovsky, S. Polesya, H. Ebert, and W. Bensch, Phys. Rev. B **94**, 184430 (2016).
[29] M. Weinert, R. E. Watson, and J. W. Davenport, Phys. Rev. B **32**, 2115 (1985).
[30] T. Oguchi and T. Shishidou, Phys. Rev. B **70**, 024412 (2004).
[31] Y. Uratani, T. Shishidou, and T. Oguchi, Journal of the Physical Society of Japan **78**, 084709 (2009).